Comparing A Heliospheric SWCX Model's Predictions To HaloSat Observations

R. Ringuette, Dimitra Koutroumpa, Kip D. Kuntz, P. Kaaret, K. Jahoda, D. Larocca, M. Kounkel, Jacob Richardson, A. Zajczyk, J. Bluem

Comparing A Heliospheric SWCX Model's Predictions To HaloSat Observations

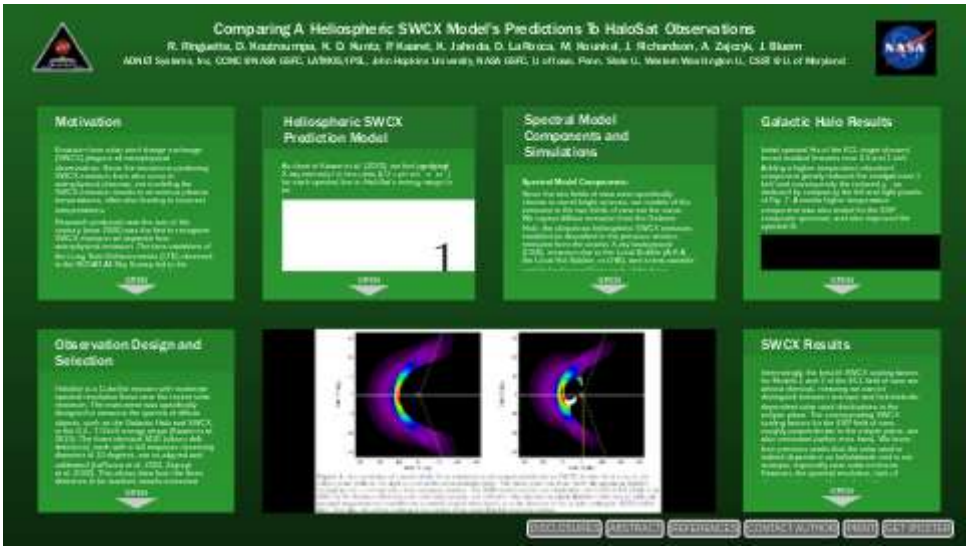

R. Ringuette, D. Koutroumpa, K. D. Kuntz, P. Kaaret, K. Jahoda, D. LaRocca, M. Kounkel, J. Richardson, A. Zajczyk, J. Bluem

ADNET Systems, Inc, CCMC @ NASA GSFC, LATMOS/IPSL, John Hopkins University, NASA GSFC, U. of Iowa, Penn. State U., Western Washington U., CSST @ U. of Maryland

PRESENTED AT:

MOTIVATION

Solar Wind Charge eXchange (SWCX) is the interaction between heavy ions in the solar wind and neutral atoms. These interactions emit radiation at a variety of wavelengths, including low-energy X-rays. Emission from SWCX plagues all astrophysical observations. Since the transitions producing SWCX emission lines also occur in astrophysical plasmas, not modeling the SWCX emission results in erroneous plasma temperatures, often also leading to incorrect interpretations.

Research produced near the turn of the century (near 2000) was the first to recognize SWCX emission as separate from astrophysical emission. The time-variations of the Long Term Enhancements (LTE) observed in the ROSAT All Sky Survey led to the correlation of the signatures with the interaction between the solar wind and the Earth's exosphere, later called magnetospheric SWCX (Freyberg 1994, 1998, Cravens et al. 2001, Cox 1998). Later work also distinguished emission originating from the Local Bubble as distinct from heliospheric SWCX, SWCX emission resulting from the interaction of the interstellar medium (ISM) with the heliosphere, resulting in a more physical size for the Local Bubble (Lallement 2004).

While magnetospheric SWCX emission in astrophysical observations can generally be avoided by instruments by choosing look directions (lines of sight) to avoid the dayside magnetosphere, heliospheric SWCX emission is ubiquitous (Kuntz 2018). Its effects on the observed spectrum are best handled through modeling of the amount of emission in the spectrum. Subsequently, models of heliospheric SWCX emission are improved by comparisons with observations, typically observations of the He cone.

The He cone is where the He originating in the ISM is gravitationally focussed by the Sun into a cone-shaped feature in the ecliptic plane. The corresponding H component in the ISM is most ionized in the inner solar system, leaving the He cone as the dominate SWCX-illuminated feature observable from Earth orbit, depicted in Fig. 1.

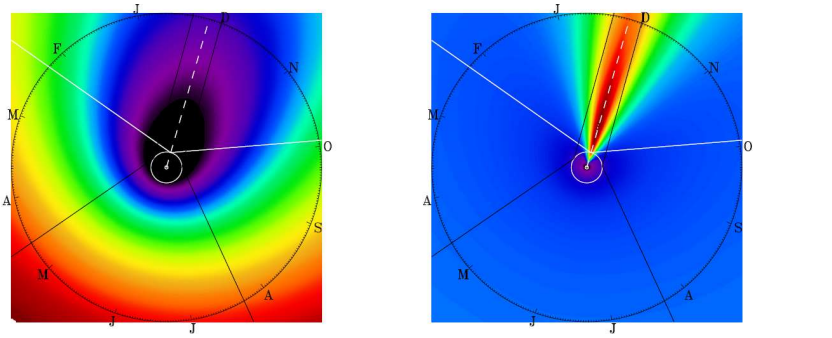

Figure 1: The distribution of neutral H (left) and neutral He (right) in the ecliptic plane. The linear scale runs from black (the minimum density) through purple to red (the maximum density). The orbit of the Earth about the Sun has been marked (small white circle), as has the part of the sky observable by *HaloSat* on 7 December (solid white lines) and ±71 days (solid black lines), the interval for which the He cone is observable by HaloSat. Our observations were made parallel to the dashed white lines. At the ±71 day locations, observations of the He cone will necessarily be through part of the magnetosheath. The outer ring has a radius of 10 au and has been marked to show the angular location of the Earth at the beginning of each month.

As evident on the diagram, the strongest signature from the He cone occurs as the Earth transits the feature in December of each year. This signature also spatially corresponds to a dearth of H. Taking into account the inverse relationship of brightness and distance, one should conclude that the dominant SWCX signal during He cone transits is from nearby He (shown in Fig 2.)

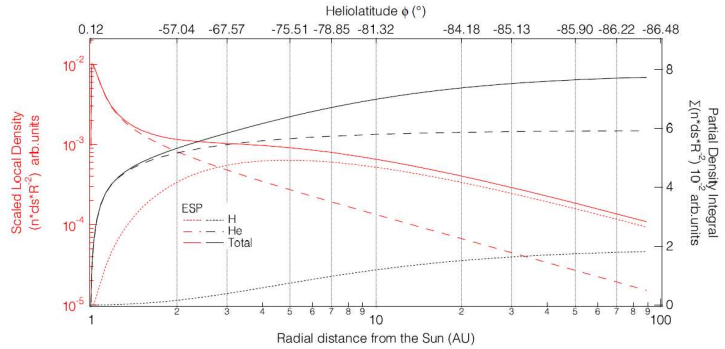

Figure 2: Qualitative function/distribution of the heliospheric SWCX emission due to charge exchange with H (dotted lines), He (dashed lines), and their total emission (solid lines) for the ecliptic south pole (ESP). In red (left axis in logarithmic scale) are shown the neutral density profiles, scaled to the R^{-2} radial distance to account for the dilution of solar wind and the spatial step (ds) along the line-of-sight of the heliospheric simulations. In black (right axis in linear scale) are shown the partial density integrals along the line-of-sight, which are proportional to the SWCX emission assuming a uniform solar wind.

Previous observations of the He cone at this time of year were performed with two flights of the DXL sounding rocket. Analysis of these observations and related work confirmed the expected X-ray signature of the He cone and refined our models of heliospheric SWCX emission (Galeazzi et al. 2014, Uprety et al. 2016). However, DXL's spectral resolution was not sufficient to resolve the emission lines above ~0.4 keV, the energy range of most modern X-ray observatories. The lack of specially designed observations of the He cone in this energy range with sufficient spectral resolution motivates this work.

For more details, please consult the corresponding paper in the Astrophysical Journal, titled *HaloSat* Observations of Heliospheric Solar Wind Charge eXchange, by Ringuette et al (2021), currently submitted for publication.

HELIOSPHERIC SWCX PREDICTION MODEL

As done in Kaaret et al. (2020), we find predicted X-ray intensity I in line units (LU = ph cm^{-2} s^{-1}sr^{-1}) for each spectral line in *HaloSat's* energy range to be

$$I_\gamma = \frac{1}{4\pi}\sum_{j=1}^{N} F_{Xq+}(\lambda_j, \beta_j, R_j) \times \qquad (1)$$
$$[N_H(\lambda_j, \beta_j, R_j)\sigma_{H,Xq+}Y_{\gamma,H} +$$
$$N_{He}(\lambda_j, \beta_j, R_j)\sigma_{He,Xq+}Y_{\gamma,He}]ds$$

where the H and He neutral distributions (N_H and N_{He}) are a function of eliptic longitude λ, ecliptic latitude β, and distance from the Sun R for each position along the line of sight, and are each calculated based on the solar wind conditions for each observation (Koutroumpa et al. 2006 and Koutroumpa 2012). The primary ion species in *HaloSat's* energy band are O^{7+}, O^{8+}, and Ne^{9+}, for which the velocity-dependent cross-sections, σ, and photon yields, Y, are relatively well-understood (Koutroumpa et al. 2007).

Since contemporary Advanced Composition Explorer (ACE) Solar Wind Ion Composition Spectrometer (SWICS, Gloeckler et al. 1998) data no longer offers measurement for these ions, the corresponding ion fluxes at each jth location were calculated using empirical models. Those for O^{7+} and O^{8+} are given in Kaaret et al. (2020), and the empirical relation for the ion flux of Ne^{9+} is of similar form.

$$F_{Ne^{9+}} = 0.2249 - 0.22609\exp(-(N_{O7+}/N_{O6+} \qquad (2)$$
$$- 0.00094032)/6.9627))$$

We test two versions of our heliospheric SWCX model. Model 1 assumes an isotropic slow solar wind with constant charge exchange cross sections. Model 2 assumes the proton flux and velocity profiles are a function of heliolatitude, which are derived from a full-sky hydrogen Ly-α map inversion analysis (Koutroumpa et al. 2019) based on data from the Solar Wind ANisotropies (SWAN; Bertaux et al. 1988) on board the Solar and Heliospheric Observatory (SOHO; Domingo et al. 1995) (e.g. left panel of Fig 5). Both models assume the ions travel at the same velocity as the protons.

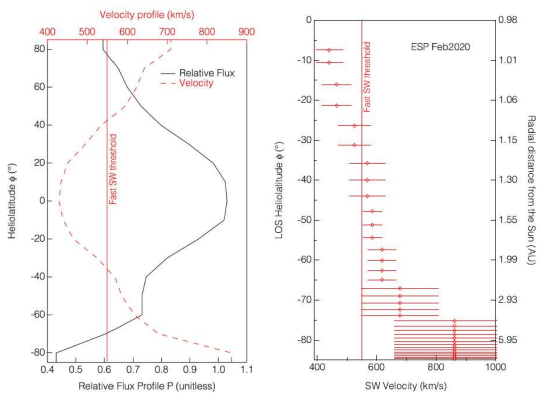

Figure 5: Solar Wind Flux and Velocity Profiles. Left: Average solar wind (SW) proton flux heliolatitude profile in 10° bins relative to the equatorial value (black curve) for the solar minimum period (2018-2020) derived from the SOHO/SWAN full-sky hydrogen Ly-α maps inversion analysis (Koutroumpa et al. 2019). Average SW velocity heliolatitude profile (red-dashed curve) derived from the same analysis. The red vertical line represents the fast SW threshold at 550 km s^{-1}, used to determine the cross-sections' dependence over latitude. Right: Local SW velocity heliolatitude profile along the line-of-sight of Feb2020 observation of the ESP, derived from the profile on the left-hand figure. The local heliolatitude of each step is marked on the left-hand axis, with the corresponding radial distance from the Sun marked on the right-hand axis. The red vertical line represents the fast SW threshold at 550 km s^{-1}.

We distinguish between "fast" and "slow" solar winds by using a threshold of 550 km/s, and use a single charge exchange cross-section for each regime. We also note the photon yield velocity dependence is very small and was not taken into account. Our velocity-dependent cross-section assumption only affects one ESP observation, as shown in the right panel of Fig 5. In this case, the fast solar wind regime influences most of the line of sight starting at ~1.2 AU.

SPECTRAL MODEL COMPONENTS AND SIMULATIONS

Spectral Model Components:

Since the two fields of view were specifically chosen to avoid bright sources, our models of the emission in the two fields of view are the same. We expect diffuse emission from the Galactic Halo, the ubiquitous heliospheric SWCX emission, modeled as described in the previous section, emission from the cosmic X-ray background (CXB), emission due to the Local Bubble (A.K.A. the Local Hot Bubble, or LHB), and a time-variable particle background from each of the three detectors. The models chosen for each component are indicated in Table 1.

Table 1: Models for each spectral component

Component Name	Model
Particle Background	*powerlaw**
Local Hot Bubble (LHB)	*apec*
Cosmic X-ray Background	*tbabs x powerlaw*
Galactic Halo	*tbabs x apec*
SWCX	*7 additive gaussians*

* One for each detector, not folded through the instrumental response matrix

Using the results in Liu et al (2017), we represent the Local Hot Bubble with a thermal component of solar metallicity and a temperature of 0.097 keV. We calculated the emission measure for *HaloSat's* field of view to be 2.17×10^{-3} and 3.25×10^{-3} pc/cm^6 for the ECL and ESP fields of view. Using the results obtained in Capelluti et al. (2017) without removing sources, we represent the cosmic X-ray background (CXB) by an absorbed powerlaw of photon index 1.45 and 1 keV normalization of 10.91 keV/cm^2/s/sr/keV. The absorption coefficient calculated for each field of view is given in Table 3 in the next section (HI4PI Collaboration 2016, Planck Collaboration 2014), as are the Galactic coordinates of both targets. We choose a metallicity of 0.3 solar for the Galactic Halo emission following the arguments in Miller & Bregman (2015) and use the same absorption coefficient as for the CXB. The redshift values for the LHB and the Galactic Halo components were set to zero. The photon indices and amplitudes of the particle backgrounds for each detector and spectrum were not fixed, as were the temperature and emission measure of the Galactic Halo component.

The SWCX emission lines discussed in the previous section are modeled using seven gaussians with the energies listed in Table 2. The energies were calculated by combining all emission lines of the same ion type within 80 eV, roughly *HaloSat's* energy resolution, using expected line ratios as weights in the resulting average. *HaloSat's* energy resolution worsens below ~0.5 eV due to a variety of factors, so we combined the dominant emission lines between 0.4 to 0.5 eV into one emission line, shown on the first row of Table 2. The line ratios given in the final column are relative to the emission line indicated. The energies and widths of each line were always fixed in the spectral fits. See Table 2 and the corresponding paper for more information (noted in 'Disclosures').

Table 2: SWCX Model Parameters.

Ion(s)	Energy (keV)	Ratio
S IX, N VI C VI, N VII	0.4434	[Q]/[O VIIa] = 0.925
O VIIa	0.5633	1.0
O VIIb	0.6792	[Q]/[O VIIa] = 0.126
O VIIIa	0.6531	1.0
O VIIIb	0.8031	[Q]/[O VIIIa] = 0.549
Ne IXa	0.9087	1.0
Ne IXb	1.1004	[Q]/[Ne IXa] = 0.100

Primary ion lines are indicated with an 'a', secondary lines with a 'b'. During spectral fitting, the low energy line is either held fixed relative to O VIIa with the given ratio, or fitted simultaneously with the other primary lines.

Simulations:

Spectral confusion between SWCX emission and astrophysical plasmas remains an issue for the current work. Low-temperature flux mistakenly assigned to the Galactic Halo (as opposed to SWCX) artificially lowers the measured temperature and raises the emission measure of the Galactic Halo. Mistaken assigments in the opposite direction have the opposite effect. In order to accurately compare the heliospheric SWCX predictions to those observed in the spectra, we must find a way to distinguish between them.

Spectral modeling using Xspec (Arnaud 1996) confirms that flux can be assigned to either the SWCX of Galactic Halo component without any residual features indicating an erroneous assignment. The only indication of a correct assignment of flux to the Galactic Halo and SWCX components is a lower χ^2. Therefore, we include a SWCX scaling factor, a fitted parameter multiplying the SWCX model of seven gaussians, in the spectral fit of the composite spectrum of the ECL and ESP targets. To reduce the complexity of the fit, we perform spectral fits for each of the composite spectra for a range of fixed SWCX scaling factors, and report the fitted parameter values for the SWCX scaling factor with the lowest χ^2 in the next section, including errors on the best-fit SWCX scaling factor.

GALACTIC HALO RESULTS

Initial spectral fits of the ECL target showed broad residual features near 0.6 and 1 keV. Adding a higher temperature absorbed component greatly reduced the residual near 1 keV and consequently the reduced χ^2, as deduced by comparing the left and right panels of Fig. 7. A similar higher temperature component was also tested for the ESP composite spectrum, and also improved the spectral fit.

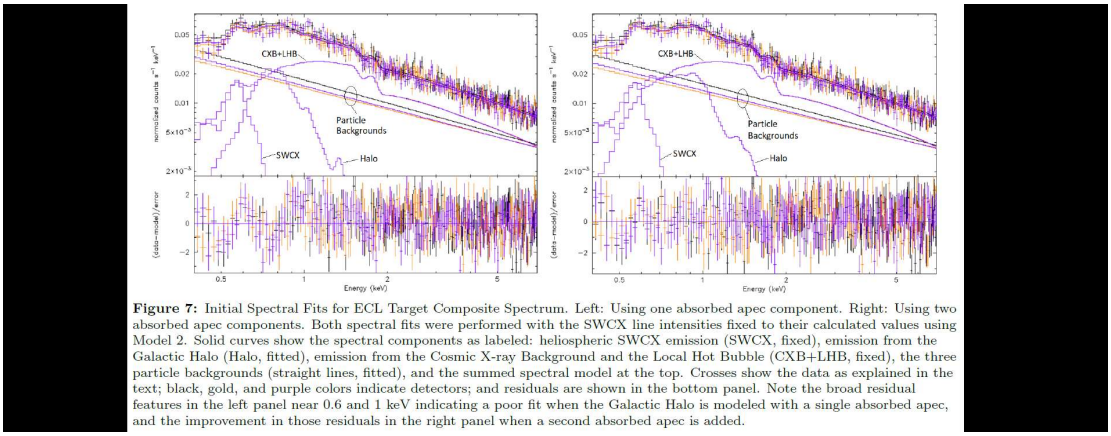

Figure 7: Initial Spectral Fits for ECL Target Composite Spectrum. Left: Using one absorbed apec component. Right: Using two absorbed apec components. Both spectral fits were performed with the SWCX line intensities fixed to their calculated values using Model 2. Solid curves show the spectral components as labeled: heliospheric SWCX emission (SWCX, fixed), emission from the Galactic Halo (Halo, fitted), emission from the Cosmic X-ray Background and the Local Hot Bubble (CXB+LHB, fixed), the three particle backgrounds (straight lines, fitted), and the summed spectral model at the top. Crosses show the data as explained in the text; black, gold, and purple colors indicate detectors; and residuals are shown in the bottom panel. Note the broad residual features in the left panel near 0.6 and 1 keV indicating a poor fit when the Galactic Halo is modeled with a single absorbed apec, and the improvement in those residuals in the right panel when a second absorbed apec is added.

The Galactic Halo temperatures and emission measures for each field of view are given in Table 3 below for the best fit SWCX-scaling factor. The lower temperature component is denoted by 'Warm-Hot', while the higher temperature component is simply labeled 'Hot'. The Warm-Hot and Hot temperatures of each target are with error bars, in contrast with the significantly different emission measures. These comparisons are also noticeable on the final spectra fits for each target, depicted in Figs. 8 and 9 below.

Table 3: Galactic Halo and SWCX Spectral Results

Description	ECL Values	ESP Values
l, b	182.7°, -16.4°	271.2°, -24.0°
$n_H (\times 10^{21} cm^{-2})$	2.48	0.661
Warm-Hot Temperature (keV)	$0.255^{+0.026}_{-0.024}$	$0.262^{+0.016}_{-0.014}$
Warm-Hot Emission Measure[a]	$9.2^{+1.8}_{-1.6}$	14.1 ± 1.6
Hot Temperature (keV)	$1.01^{+0.13}_{-0.11}$	$1.03^{+0.23}_{-0.19}$
Hot Emission Measure[a]	$2.78^{+0.53}_{-0.54}$	$1.46^{+0.76}_{-0.75}$
Exposure (ks)	292.0	107.4
Degrees of Freedom	566	300
χ^2_v	1.099	1.017
Model 1 Scaling Factor (1σ)	$1.09^{+0.22}_{-0.27}$	$2.63^{+0.56}_{-0.61}$
Model 2 Scaling Factor (1σ)	$1.06^{+0.22}_{-0.26}$	$3.80^{+0.80}_{-0.88}$

[a]Emission measure in units of $\times 10^{-3}$ cm^{-6} pc. All errors are 90% confidence intervals unless otherwise noted. The Galactic Halo temperatures and emission measures are reported with the SWCX scaling factor held fixed to the best fit value.

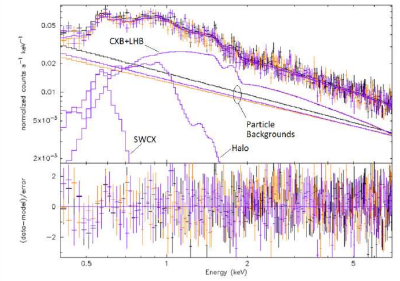

Figure 8: Spectral Fit for ECL Target Composite Spectrum. The Model 2 SWCX line intensities were scaled by the best fit factor (see text). Solid curves show the spectral components as labeled: heliospheric SWCX emission (SWCX, fixed), emission from the Galactic Halo (Halo, fitted), emission from the CXB and LHB (CXB+LHB, fixed), the three particle backgrounds (straight lines, fitted), and the total spectral model at the top. Crosses show the data; black, gold, and purple colors indicate detectors; and residuals are shown in the bottom panel. The Ne IX SWCX contributions are not visible on this scale.

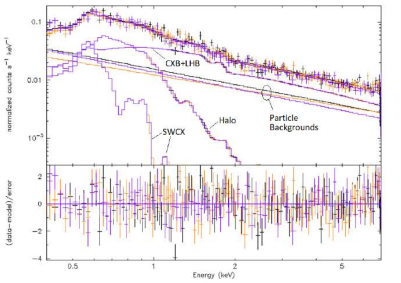

Figure 9: Spectral Fit for the ESP Composite Spectrum. The Model 2 SWCX line intensities were scaled by the best fit factor (see text). Solid curves show the spectral components as labeled: heliospheric SWCX emission (SWCX, fixed), emission from the Galactic Halo (Halo, fitted), emision from the CXB and LHB (CXB+LHB, fixed), the three particle backgrounds (straight lines, fitted), and the total spectral model at the top. Crosses show the data; black, gold, and purple colors indicate detectors; and residuals are shown in the bottom panel.

The higher temperature component was significantly detected in the ECL field of view by 8.5σ, with a marginally significant detection in the ESP field of view by 3.2σ.

Emission from young T Tauri or dwarf M stars may explain such emission in an otherwise dark field of view. But, no T Tauri stars were observed in either field of view by the GAIA DR2 survey (Kounkel & Covey 2019; Luhman 2018). Given both fields of view are more than 5 degrees from the ecliptic plane, a significant dwarf M component is also not expected (Masui et al. 2009). We propose the emission could be from diffuse gas ~10^7 K in the Galactic Halo along the line of sight.

OBSERVATION DESIGN AND SELECTION

HaloSat is a CubeSat mission with moderate spectral resolution flown near the recent solar minimum. The instrument was specifically designed to measure the spectra of diffuse objects, such as the Galactic Halo and SWCX, in the 0.4 - 7.0 keV energy range (Kaaret et al. 2019). The three identical SDD (silicon drift detectors), each with a full response observing diameter of 10 degrees, are co-aligned and calibrated (LaRocca et al. 2020, Zajczyk
et al. 2020). This allows data from the three detectors to be stacked, greatly improving statistics.

HaloSat's observing strategy avoided bright sources, lines of sight within 90 degrees of the Sun from its low Earth orbit, and daytime observations (Kuntz 2018). The observations used for this work were specifically designed as follows. Two fields of view were chosen without bright sources to observe the He cone along the ecliptic, called ECL, and roughly perpendicular to it, called ESP for its proximity to the ecliptic south pole. Observations of these two targets were attempted monthly during two seven month spans, each centered on Earth's transit of the He cone in early December (2018-2020). Fig 1 (repeated below) indicates the direction of our observations with the dashed white lines.

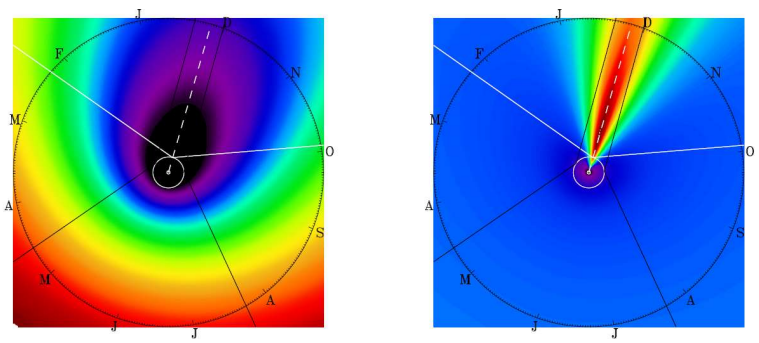

Figure 1: The distribution of neutral H (left) and neutral He (right) in the ecliptic plane. The linear scale runs from black (the minimum density) through purple to red (the maximum density). The orbit of the Earth about the Sun has been marked (small white circle), as has the part of the sky observable by *HaloSat* on 7 December (solid white lines) and ±71 days (solid black lines), the interval for which the He cone is observable by HaloSat. Our observations were made parallel to the dashed white lines. At the ±71 day locations, observations of the He cone will necessarily be through part of the magnetosheath. The outer ring has a radius of 10 au and has been marked to show the angular location of the Earth at the beginning of each month.

Completely avoiding magnetospheric SWCX in the observations was not always possible, but turned out not to be problematic. Fig 3 shows an example of the modeled magnetospheric SWCX emission during one such observation in two slices in the GSE plane. The majority of the ECL lines of sight were between the white lines in each image, avoiding significant contribution in the spectra from magnetospheric SWCX. However, observations of the ESP were constrained by *HaloSat's* observation restrictions to always be through a dim portion of the emission, indicated by the yellow line in the right image. As we report later, the emission predicted by a BATS-R-US (T□oth et al. 2005) model for those observations were below *HaloSat's* sensitivity, and thus did not significantly affect the spectra.

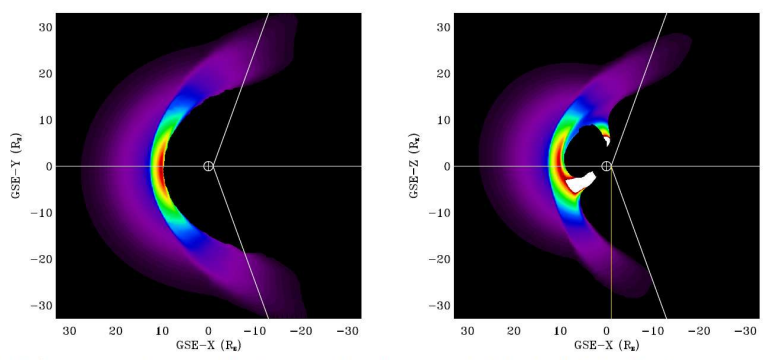

Figure 3: A cross-section of a model of the X-ray emissivity in the magnetosheath due to SWCX. On the left is a cut in the ecliptic plane while on the right is a cut in the noon-midnight plane. The linear scale runs from black (the minimum density) through purple to red and white (the maximum density). The MHD model used for this illustration was BATS-R-US (Tóth et al. 2005) for 03 December 2018 when the solar wind pressure was 1.96 nPa. The direction in which *HaloSat* could observe with only marginal magnetospheric contribution is marked (angled white lines), as is the direction of the ecliptic south pole (ESP) (yellow line). Note that the ecliptic south pole lies outside of the usual *HaloSat* observing window.

High count rates in a high energy band, 3-7 keV, were used to filter out observations with high particle backgrounds, and distinguish between low-background observations and acceptable observations. The low background observations of each target were combined into one composite spectrum of each target for

determination of the non-time-varying spectral components (e.g. the cosmic X-ray background and the Galactic Halo emission). The low and acceptable background observations of each target were also sorted into groups by target, observation date, and the high energy band count rate for measuring the time-varying heliospheric SWCX contribution of the He cone. Grouping the individual observations by these categories resulted in eight (8) spectra of the ECL and five (5) spectra of the ESP. Further details on the analysis of composite and grouped spectra are given in the last two sections of this poster.

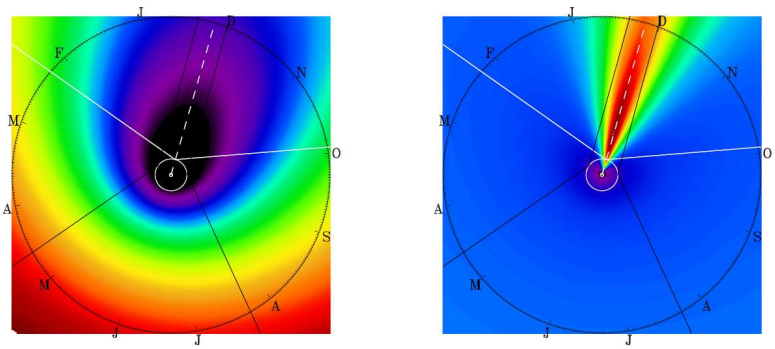

Figure 1: The distribution of neutral H (left) and neutral He (right) in the ecliptic plane. The linear scale runs from black (the minimum density) through purple to red (the maximum density). The orbit of the Earth about the Sun has been marked (small white circle), as has the part of the sky observable by *HaloSat* on 7 December (solid white lines) and ±71 days (solid black lines), the interval for which the He cone is observable by HaloSat. Our observations were made parallel to the dashed white lines. At the ±71 day locations, observations of the He cone will necessarily be through part of the magnetosheath. The outer ring has a radius of 10 au and has been marked to show the angular location of the Earth at the beginning of each month.

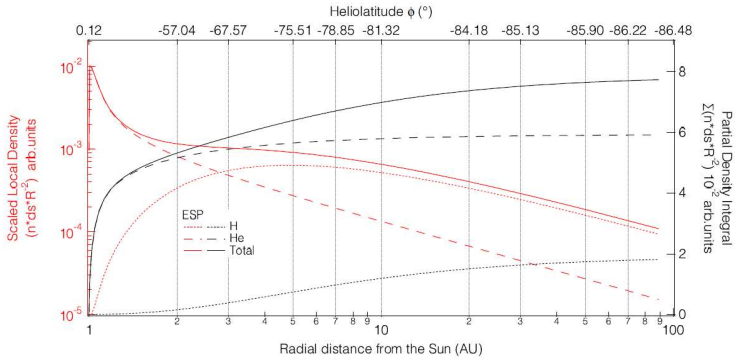

Figure 2: Qualitative function/distribution of the heliospheric SWCX emission due to charge exchange with H (dotted lines), He (dashed lines), and their total emission (solid lines) for the ecliptic south pole (ESP). In red (left axis in logarithmic scale) are shown the neutral density profiles, scaled to the R^{-2} radial distance to account for the dilution of solar wind and the spatial step (ds) along the line-of-sight of the heliospheric simulations. In black (right axis in linear scale) are shown the partial density integrals along the line-of-sight, which are proportional to the SWCX emission assuming a uniform solar wind.

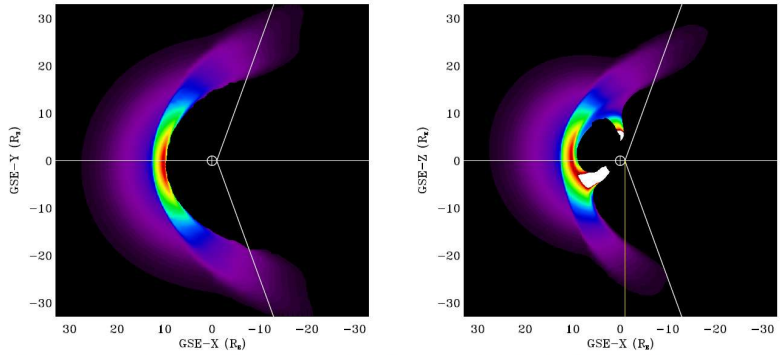

Figure 3: A cross-section of a model of the X-ray emissivity in the magnetosheath due to SWCX. On the left is a cut in the ecliptic plane while on the right is a cut in the noon-midnight plane. The linear scale runs from black (the minimum density) through purple to red and white (the maximum density). The MHD model used for this illustration was BATS-R-US (Tóth et al. 2005) for 03 December 2018 when the solar wind pressure was 1.96 nPa. The direction in which *HaloSat* could observe with only marginal magnetospheric contribution is marked (angled white lines), as is the direction of the ecliptic south pole (ESP) (yellow line). Note that the ecliptic south pole lies outside of the usual *HaloSat* observing window.

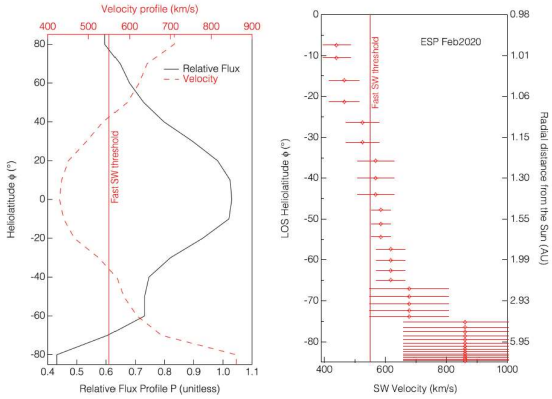

Figure 5: Solar Wind Flux and Velocity Profiles. Left: Average solar wind (SW) proton flux heliolatitude profile in 10° bins relative to the equatorial value (black curve) for the solar minimum period (2018-2020) derived from the SOHO/SWAN full-sky hydrogen Ly-α maps inversion analysis (Koutroumpa et al. 2019). Average SW velocity heliolatitude profile (red-dashed curve) derived from the same analysis. The red vertical line represents the fast SW threshold at 550 km s^{-1}, used to determine the cross-sections' dependence over latitude. Right: Local SW velocity heliolatitude profile along the line-of-sight of Feb2020 observation of the ESP, derived from the profile on the left-hand figure. The local heliolatitude of each step is marked on the left-hand axis, with the corresponding radial distance from the Sun marked on the right-hand axis. The red vertical line represents the fast SW threshold at 550 km s^{-1}.

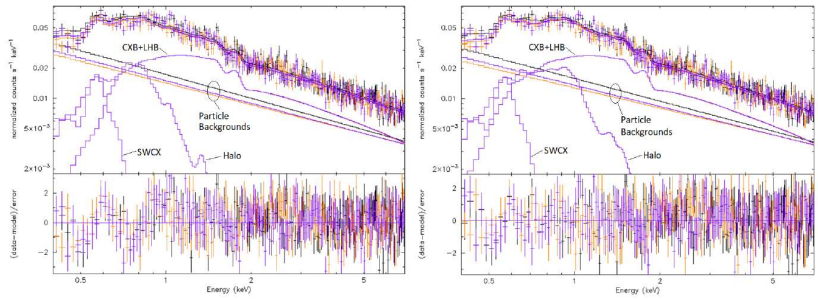

Figure 7: Initial Spectral Fits for ECL Target Composite Spectrum. Left: Using one absorbed apec component. Right: Using two absorbed apec components. Both spectral fits were performed with the SWCX line intensities fixed to their calculated values using Model 2. Solid curves show the spectral components as labeled: heliospheric SWCX emission (SWCX, fixed), emission from the Galactic Halo (Halo, fitted), emission from the Cosmic X-ray Background and the Local Hot Bubble (CXB+LHB, fixed), the three particle backgrounds (straight lines, fitted), and the summed spectral model at the top. Crosses show the data as explained in the text; black, gold, and purple colors indicate detectors; and residuals are shown in the bottom panel. Note the broad residual features in the left panel near 0.6 and 1 keV indicating a poor fit when the Galactic Halo is modeled with a single absorbed apec, and the improvement in those residuals in the right panel when a second absorbed apec is added.

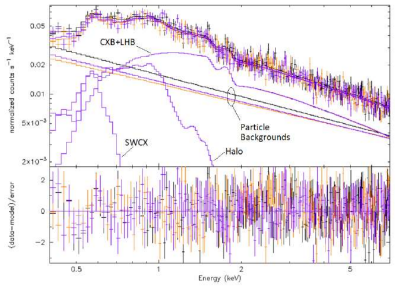

Figure 8: Spectral Fit for ECL Target Composite Spectrum. The Model 2 SWCX line intensities were scaled by the best fit factor (see text). Solid curves show the spectral components as labeled: heliospheric SWCX emission (SWCX, fixed), emission from the Galactic Halo (Halo, fitted), emission from the CXB and LHB (CXB+LHB, fixed), the three particle backgrounds (straight lines, fitted), and the total spectral model at the top. Crosses show the data; black, gold, and purple colors indicate detectors; and residuals are shown in the bottom panel. The Ne IX SWCX contributions are not visible on this scale.

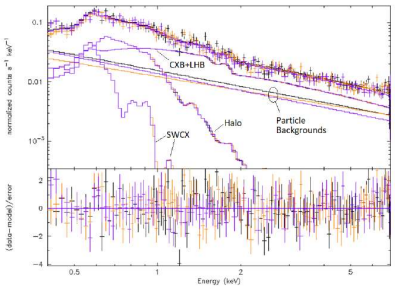

Figure 9: Spectral Fit for the ESP Composite Spectrum. The Model 2 SWCX line intensities were scaled by the best fit factor (see text). Solid curves show the spectral components as labeled: heliospheric SWCX emission (SWCX, fixed), emission from the Galactic Halo (Halo, fitted), emision from the CXB and LHB (CXB+LHB, fixed), the three particle backgrounds (straight lines, fitted), and the total spectral model at the top. Crosses show the data; black, gold, and purple colors indicate detectors; and residuals are shown in the bottom panel.

Table 2: SWCX Model Parameters.

Ion(s)	Energy (keV)	Ratio
S IX, N VI C VI, N VII	0.4434	[Q]/[O VIIa] = 0.925
O VIIa	0.5633	1.0
O VIIb	0.6792	[Q]/[O VIIa] = 0.126
O VIIIa	0.6531	1.0
O VIIIb	0.8031	[Q]/[O VIIIa] = 0.549
Ne IXa	0.9087	1.0
Ne IXb	1.1004	[Q]/[Ne IXa] = 0.100

Primary ion lines are indicated with an 'a', secondary lines with a 'b'. During spectral fitting, the low energy line is either held fixed relative to O VIIa with the given ratio, or fitted simultaneously with the other primary lines.

Table 3: Galactic Halo and SWCX Spectral Results

Description	ECL Values	ESP Values
l, b	182.7°, -16.4°	271.2°, -24.0°
$n_H (\times 10^{21} cm^{-2})$	2.48	0.661
Warm-Hot Temperature (keV)	$0.255^{+0.026}_{-0.024}$	$0.262^{+0.016}_{-0.014}$
Warm-Hot Emission Measure[a]	$9.2^{+1.8}_{-1.6}$	14.1 ± 1.6
Hot Temperature (keV)	$1.01^{+0.13}_{-0.11}$	$1.03^{+0.23}_{-0.19}$
Hot Emission Measure[a]	$2.78^{+0.53}_{-0.54}$	$1.46^{+0.76}_{-0.75}$
Exposure (ks)	292.0	107.4
Degrees of Freedom	566	300
χ^2_υ	1.099	1.017
Model 1 Scaling Factor (1σ)	$1.09^{+0.22}_{-0.27}$	$2.63^{+0.56}_{-0.61}$
Model 2 Scaling Factor (1σ)	$1.06^{+0.22}_{-0.26}$	$3.80^{+0.80}_{-0.88}$

[a]Emission measure in units of $\times 10^{-3}$ cm^{-6} pc. All errors are 90% confidence intervals unless otherwise noted. The Galactic Halo temperatures and emission measures are reported with the SWCX scaling factor held fixed to the best fit value.

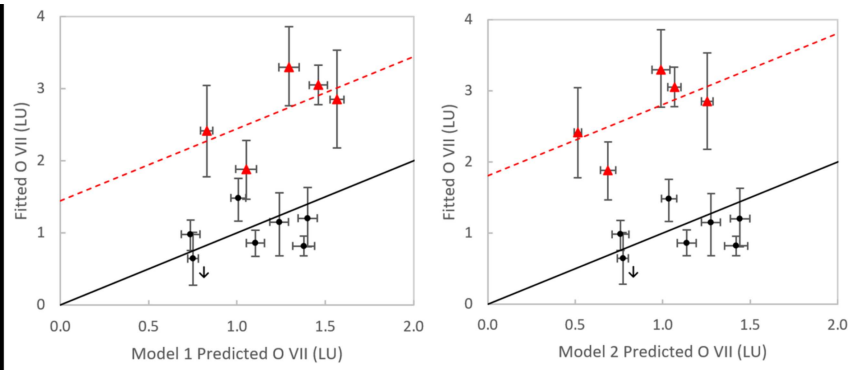

Figure 10: Measured vs Predicted O VII Fluxes. Top: Model 1 Predictions. Bottom: Model 2 Predictions. The plotted values are given with 1σ errors. The ECL and ESP data are differentiated by the black circles and red triangles, respectively. The upper limit for the Mar2020 ECL observation is shown by the black arrow. The solid lines in each plot indicate a 1:1 relationship, and the dashed lines give a 1:1 relationship for the ESP data with a fitted offset from each model.

SWCX RESULTS

Interestingly, the best-fit SWCX scaling factors for Models 1 and 2 of the ECL field of view are almost identical, meaning we cannot distinguish between isotropic and heliolatitude-dependent solar wind distributions in the ecliptic plane. The corresponding SWCX scaling factors for the ESP field of view, roughly perpendicular to the ecliptic plane, are also consistent (within error bars). We know from previous works that the solar wind is indeed dependent on heliolatitude and is not isotropic, especially near solar minimum. However, the spectral resolution, lack of observing time, and level of particle background in the observations we obtained are not sufficient to arrive at this conclusion.

Once the best-fit SWCX scaling factor and Galactic Halo parameters were determined, we then analyzed the grouped spectra, described in the 'Observation Design and Selection' section, in the following manner. Each grouped spectra presents a measurement of the same astrophysical parameters in each spectrum of that field of view plus a measurement of the SWCX emission along the line of sight at that time on top of the particle backgroun. The astrophysical emission is constant on these timescales (~2 years), the SWCX emission depends on the variables described in the 'Heliospheric SWCX Prediction Model' section (including the line of sight), and the particle background varies on very short timescales. Therefore, we fixed the astrophysical parameters to the values in Table 3, allowed the particle backgrounds to be fitted as before, and simultaneously fit for the amplitude of the SWCX emission as represented by the low energy, O VII, O VIII, and Ne IX lines.

Due mainly to the low exposure times and the presence of the particle backgrounds, we were only able to significantly detect emission from the O VII line in each grouped spectrum. In Fig 10, we plot the observed O VII line intensity for each grouped spectrum against the value predicted by the heliospheric SWCX model. The black diagonal line represents the hypothesis of a set of predictions equal to the observations. Points above this line represent underpredicted values, while points below this line represent overpredicted values.

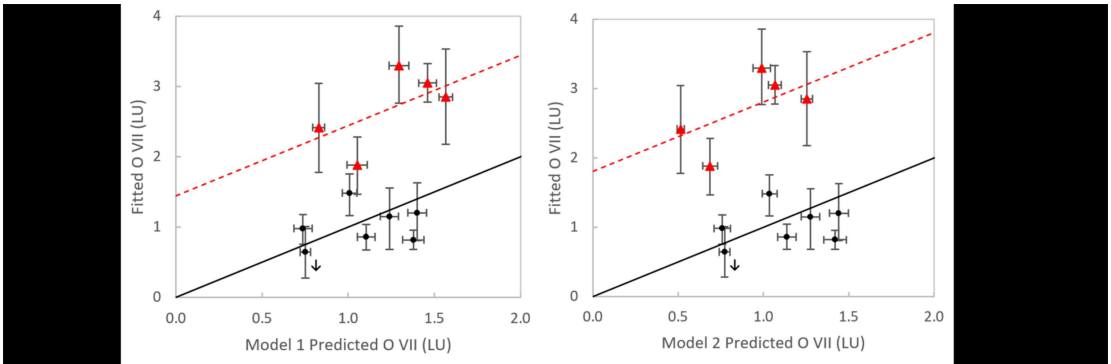

Figure 10: Measured vs Predicted O VII Fluxes. Top: Model 1 Predictions. Bottom: Model 2 Predictions. The plotted values are given with 1σ errors. The ECL and ESP data are differentiated by the black circles and red triangles, respectively. The upper limit for the Mar2020 ECL observation is shown by the black arrow. The solid lines in each plot indicate a 1:1 relationship, and the dashed lines give a 1:1 relationship for the ESP data with a fitted offset from each model.

As is evident in the figure, the ESP observations are consistently underpredicted with a X^2/dof of 37.315/5 for Model 1 and 22.438/5 for Model 2, while the ECL observations are well predicted (X^2/dof of 4.930/8 for Model 1, and 5.352/8 for Model 2). This underprediction translates into 0.8-2.0 LU of O VII emission not accounted for by either of our models. Also puzzling is the somewhat large values of the best-fit SWCX scaling factor for the ESP field of view. Therefore, we investigated other possible sources of this emission for the ESP observations.

Given the lines of sight for the ESP observations were necessarily through a portion of the magnetosheath, we modeled the expected magnetospheric SWCX emission for each ESP observation. Similar to the O VII intensity equation given in the 'Heliospheric SWCX Prediction Model' section, the magnetospheric contribution can be calculated by

$$I = \frac{1}{4\pi}\int_{obs}^{\infty} F_{O+7}(s) N_H(s) \sigma_{H,O+7} Y_{OVII,H} ds \qquad (3)$$

$$= \frac{1}{4\pi}\frac{N_{O+7}}{N_P}\int_{obs}^{\infty} N_P(s) V_P(s) N_H(s) \sigma_{H,O+7} Y_{OVII,H} ds$$

which assumes the change exchange interactions occurring in the magnetosheath are predominately with H. Using the services of the CCMC at NASA's Goddard Space Flight Center, we acquired a BATS-R-US (T□oth et al. 2005) MHD simulation for each observation using temporaneous solar wind pressure extracted from OMNI data (King & Papitashvili 2005), and correctly tracking the Earth's dipole tilt. Of the ESP grouped observations, the maximum possible magnetospheric SWCX contribution of 0.08 LU is still a factor of 10 below the minimum difference reported earlier. Therefore, we conclude that magnetospheric SWCX contribution in the spectra obtained cannot explain the excess O VII emission observed.

We also performed simulations of possible O I contribution at 525 keV to the spectra, which could possibly be confused with O VII emission in the analysis due to the small difference in energies. Such emission would result from lines of sight through the outer portions of the Earth's atmosphere which contain ionized oxygen (Ezoe et al. 2011, Sekiya et al. 2014). However, removing data with bright earth limb angles below 175 degrees, corresponding to 19.8 ks, did not reduce the best-fit SWCX scaling factor for the ESP field of view. Spectral simulations representing an additional O I component in the ESP composite spectrum also failed to produce the elevated SWCX scaling factor. Instead, the simulations produced a SWCX scaling factor consistent with zero and a residual excess at the O I energy, niether of which are observed in the ESP composite spectral fit. Therefore, we also conclude that O I contamination from the Earth's atmosphere does not explain the excess O VII emission observed in the ESP spectra.

We hesitantly suggest that the excess emission may be due to either increased CME activity in the southern hemisphere, although no particular event may be linked to our observations, an incomplete model of the solar wind at high latitudes, or physical processes we do not yet understand. Additional simultaneous observations in the ecliptic plane and roughly towards the ecliptic poles during transits of the He cone are imperative to further investigate this discrepancy.

ABSTRACT

Every astrophysical observation is contaminated by X-ray emission from solar wind charge exchange (SWCX), which complicates measurements of astrophysical plasma properties. However, predicting the spectral shape and amplitude of the emission in each observation remains a challenge due to the unknown local solar wind fluxes along the line of sight, and the large uncertainties in the charge exchange cross sections of the various participating ions and neutrals. Recent specialized observations of the He cone, a strong heliospheric SWCX emission feature, have been completed by *HaloSat*, an X-ray CubeSat mission. In this poster, we compare predictions of a heliospheric SWCX emission model with the data obtained by *HaloSat* at low and high ecliptic latitudes during two transits of the He cone. The SWCX emission amplitudes predicted by the model were consistent with the observations at low ecliptic latitude, which is not surprising given the solar wind data is monitored in the same plane at L1. However, the measured values near the ecliptic south pole were under-predicted by the model, and additionally not explained by foreseeable contributors. We also report absorbed high temperature emission for both spectral sets, possibly due to a high temperature component in the Galactic Halo.

REFERENCES

Arnaud, K. A. 1996, in Astronomical Data Analysis Software and Systems V, ASP, ed. J. H. Jacoby & J. Barnes, 17-20

Bertaux, J. L., Pellinen, R., Chasse ere, E., et al. 1988, in The SOHO Mission. Scientific and Technical Aspects of the Instruments, 63-68

Cappelluti, N., Li, Y., Ricarte, A., et al. 2017, ApJ, 837, 19

Collaboration, H. 2016, A&A, 594, A116

Collaboration, P. 2014, A&A, 571, A13

Cox, D. P. 1998, in Lecture Notes in Physics, Berlin, Springer Verlag, Vol. 506, IAU Colloq. 166: The Local Bubble and Beyond, ed. D. Breitschwerdt, M. J. Freyberg, & J. Truemper, 121-131

Cravens, T. E., Robertson, I. P., & Snowden, S. L. 2001, J. Geophys. Res., 106, 24883

Domingo, V., Fleck, B., & Poland, A. I. 1995, Space Sci. Rev., 72, 81

Ezoe, Y., Miyoshi, Y., Yoshitake, H., et al. 2011, PASJ, 63, S691

Freyberg, M. J. 1994, PhD thesis, Technische Univ. M unchen, (1994)

---. 1998, in Lecture Notes in Physics, Berlin Springer Verlag, Vol. 506, IAU Colloq. 166: The Local Bubble and Beyond, ed. D. Breitschwerdt, M. J. Freyberg, & J. Truemper, 113-116

Galeazzi, M., Chiao, M., Collier, M. R., et al. 2014, Nature, 512, 171

Gloeckler, G., Cain, J., Ipavich, F. M., et al. 1998, in The Advanced Composition Explorer Mission (Springer Netherlands), 497-539

Kaaret, P., Zajczyk, A., LaRocca, D. M., et al. 2019, ApJ, 884, 162

Kaaret, P., Koutroumpa, D., Kuntz, K., et al. 2020, Nature Astronomy

Koutroumpa, D., Qu emerais, E., Ferron, S., & Schmidt, W. 2019, Geophys. Res. Let., 46, 4114

Koutroumpa, D. 2012, Astron. Nachr., 333, 341

Koutroumpa, D., Acero, F., Lallement, R., Ballet, J., & Kharchenko, V. 2007, A&A, 475, 901

Koutroumpa, D., Lallement, R., Kharchenko, V., et al. 2006, A&A, 460, 289

Kuntz, K. D. 2018, A&AR, 27, doi:10.1007/s00159-018-0114-0

Lallement, R., Raymond, J. C., Vallerga, J., et al. 2004, A&A, 426, 875

LaRocca, D. M., Kaaret, P., Kirchner, D. L., et al. 2020, JATIS, 6, 1

Liu, W., Chiao, M., Collier, M. R., et al. 2017, ApJ, 834, 33

Luhman, K. L. 2018, AJ, 156, 271

Masui, K., Mitsuda, K., Yamasaki, N. Y., et al. 2009, PASJ, 61, S115

Miller, M. J., & Bregman, J. N. 2015, ApJ, 800, 14

Sekiya, N., Yamasaki, N. Y., Mitsuda, K., & Takei, Y. 2014, PASJ, 66, L3

T oth, G., Sokolov, I. V., Gombosi, T. I., et al. 2005, J. Geophys. Res., 110

Uprety, Y., Chiao, M., Collier, M. R., et al. 2016, ApJ, 829, 9

Zajczyk, A., Kaaret, P., LaRocca, D., et al. 2020, JATIS, 6, doi:10.1117/1.jatis.6.4.044005